



CHALMERS
UNIVERSITY OF TECHNOLOGY

Role of Interfacial Defects on Electro–Chemo–Mechanical Failure of Solid-State Electrolyte

Downloaded from: <https://research.chalmers.se>, 2023-07-15 08:16 UTC

Citation for the original published paper (version of record):

Liu, Y., Xu, X., Jiao, X. et al (2023). Role of Interfacial Defects on Electro–Chemo–Mechanical Failure of Solid-State Electrolyte. *Advanced Materials*, In Press.
<http://dx.doi.org/10.1002/adma.202301152>

N.B. When citing this work, cite the original published paper.

Role of Interfacial Defects on Electro–Chemo–Mechanical Failure of Solid-State Electrolyte

Yangyang Liu, Xieyu Xu, Xingxing Jiao, Olesya O. Kapitanova, Zhongxiao Song, and Shizhao Xiong*

High-stress field generated by electroplating of lithium (Li) in pre-existing defects is the main reason for mechanical failure of solid-state electrolyte because it drives crack propagation in electrolyte, followed by Li filament growth inside and even internal short-circuit if the filament reaches another electrode. To understand the role of interfacial defects on mechanical failure of solid-state electrolyte, an electro–chemo–mechanical model is built to visualize distribution of stress, relative damage, and crack formation during electrochemical plating of Li in defects. Geometry of interfacial defect is found as dominating factor for concentration of local stress field while semi-sphere defect delivers less accumulation of damage at initial stage and the longest failure time for disintegration of electrolyte. Aspect ratio, as a key geometric parameter of defect, is investigated to reveal its impact on failure of electrolyte. Pyramidic defect with low aspect ratio of 0.2–0.5 shows branched region of damage near interface, probably causing surface pulverization of solid-state electrolyte, whereas high aspect ratio over 3.0 will trigger accumulation of damage in bulk electrolyte. The correction between interfacial defect and electro–chemo–mechanical failure of solid-state electrolyte is expected to provide insightful guidelines for interface design in high-power-density solid-state Li metal batteries.

1. Introduction


Rechargeable solid-state lithium-metal batteries (SSLMBs) that are composed of solid-state electrolyte and lithium (Li) metal anode show a great promise for massive application of battery systems with enhanced energy density and high safety, which are expected to break the bottlenecks limiting advance of the state-of-the-art Li-ion batteries.^[1–3] However, the maximum tolerable current density of present SSLMBs under practical conditions is usually $<0.5 \text{ mA cm}^{-2}$ and it is far below the requirement of power batteries for transportation industry ($>4 \text{ mA cm}^{-2}$), hindering the yield of sufficient power capability from SSLMBs for electric vehicles.^[4,5] The cell failure caused by an internal short-circuit will be inevitably triggered once the SSLMBs operate above a critical current density (CCD).^[6–8] It is generally accepted that the internal short-circuit is created by the growth and propagation of Li filaments inside solid-state electrolyte, resulting in the electrical connection between cathode with Li anode.^[9–14]

To reveal the mechanism for Li penetration in solid-state electrolyte, advanced characterizing techniques were employed to capture the Li nucleation at electrolyte/Li anode interface, growth of Li filaments and mechanical failure of solid-state electrolyte.^[10,12,15–17] Based on these results, there are two typical mechanisms proposed for the electro–chemo–mechanical failure of solid-state electrolyte induced by growth of Li dendrites inside. One is the penetration/infiltration of plated Li into pre-existing defects on the electrolyte surface^[9] and another one is reduction of Li in the bulk of solid-state electrolyte at internal locations with high electronic conductivity.^[16,18] Our previous work reveals the mechanical failure of solid-state electrolyte induced by internal growth of Li filaments with various sizes and number densities,^[19] leaving another mechanism for penetration/infiltration of Li from interfacial defects. Operando video microscopy analysis of cross section in Li symmetric cell with solid-state electrolyte shows that nucleation of Li filaments at interface was immediately monitored when the applied current density was over CCD and the rapid propagation of Li filaments in solid-state electrolyte ultimately leads to the short-circuit of cell.^[15] Moreover, employment of in situ X-ray tomography coupled with spatially mapped X-ray diffraction reveals the

Y. Liu, X. Xu, X. Jiao, O. O. Kapitanova, Z. Song
State Key Laboratory for Mechanical Behavior of Materials
Xi'an Jiaotong University
Xi'an 710049, P. R. China

Z. Song
Engineering Research Center of Energy Storage Materials and Devices
Ministry of Education
Xi'an Jiaotong University
Xi'an 710049, P. R. China

S. Xiong
Department of Physics
Chalmers University of Technology
Göteborg SE 412 96, Sweden
E-mail: shizhao.xiong@chalmers.se

 The ORCID identification number(s) for the author(s) of this article can be found under <https://doi.org/10.1002/adma.202301152>

© 2023 The Authors. Advanced Materials published by Wiley-VCH GmbH. This is an open access article under the terms of the Creative Commons Attribution License, which permits use, distribution and reproduction in any medium, provided the original work is properly cited.

DOI: 10.1002/adma.202301152

formation of defects at interface, propagation of Li filament from Li anode to another electrode and the mechanical failure of solid-state electrolyte.^[10–12] It is found that the crack within solid-state electrolyte was created ahead of Li filaments during the plating process and initiates near the surface of plated Li anode, paving the pathway for the propagation of Li filament.^[12] The further propagation of Li filament following cracks leads to the internal short-circuit of solid-state cells. This finding explains well why a solid-state electrolyte with sufficient shear modulus (8.3 GPa for amorphous Li₂S-P₂S₅ and 61 GPa for oxide garnet)^[9] fails to suppress the propagation of Li filament inside which only has a shear modulus of 2.8 GPa.^[20]

The locally high stress field generated by the electroplating of Li in interfacial defects/flaws is proposed as the main reason for the germination of cracks near the plated Li anode.^[9,11,12] The interfacial defects, like voids, impurities, and high roughness, are widely present at the surface of solid-state electrolyte due to the manufacturing processes and repeated plating/stripping process.^[4,21–23] These defects at Li/solid-state electrolyte interface will be first filled during the electrodeposition of Li occurring at the interface between solid-state electrolyte and Li anode since interfacial defects also provide high tendency of Li nucleation and high local Li ion flux.^[9,24,25] Once they are fully filled by deposited Li, the mechanical stress induced by a relatively small overpotential for subsequent plating will be sufficient to result in the Griffith-like crack extension in brittle solid-state electrolyte.^[4,24] Previous results show that the geometry and size of interfacial defects are critical parameters for the crack extension inside solid-state electrolyte during Li plating, but it is difficult to capture this evolution process which involves both electrochemical and mechanical processes.^[9,24,26,27] Therefore, understanding the role of interfacial defects on the initiation of cracks in solid-state electrolyte is of central importance for investigating the failure mechanism induced by Li penetration and developing targeted strategies to achieve high CCD in solid-state batteries.

In this work, an electro–chemo–mechanical model describing the fracture process of solid-state electrolyte (NASICON-type, Li_{1.3}Al_{0.3}Ge_{1.7}(PO₄)₃, LAGP) at the location of interfacial defect is built to visualize the local stress and resulted damage during the electroplating process of Li. This is because NASICON-type of solid-state electrolytes has been chosen as one of the most promising electrolyte materials for SSLMBs.^[28] The method of multiphysics simulation allows to track the evolution of stress at the Li/solid-state electrolyte interface, particularly surrounding the area of defect, as a result of continuous Li deposition at the interface. The formation and accumulation of damage caused by high stress at local region is further shown to reveal the key step for the initiation of cracks in solid-state electrolyte. Moreover, the propagation of cracks from interfacial defects to the bulk of electrolyte is observed, demonstrating the deep reason for the mechanical degradation of solid-state electrolyte triggered by its surface defects. Here, the geometry and aspect ratio of interfacial defects are examined to correlate their intrinsic properties with the electro–chemo–mechanical failure of solid-state electrolyte, inspiring the potential solutions of suppressing this failure by regulating the surface of electrolyte. Our work provides a comprehensive understanding of the mechanical failure of solid-state electrolyte caused by interfacial defects, showing the promise

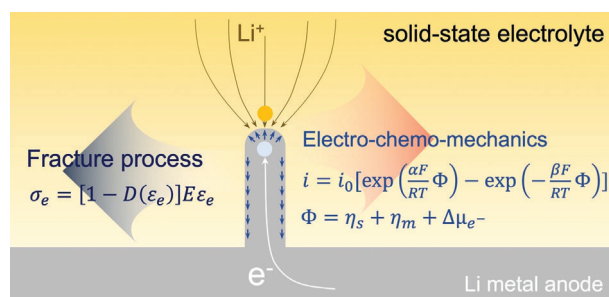


Figure 1. Schematic diagram of electro–chem–mechanical model for the fracture process of solid-state electrolyte with interfacial defect. The brown arrows in solid-state electrolyte and the white arrows in Li metal anode represent the Li-ion flux and the current through the electrode, respectively. The blue arrows are corresponding to the compressive stress at tip of Li filaments and the shear stress at interface, which are generated by continuous electrodeposition of Li.

to achieve high-power-density solid-state batteries by design of solid-state electrolyte surface.

2. Numerical Model

To simulate the failure of solid-state electrolyte caused by the electrodeposition of Li in interfacial defect, the electro–chem–mechanical process is described as two main bodies, electrochemical plating of Li and mechanical fracture process of solid-state electrolyte. As shown in **Figure 1**, the electrodeposition of Li at the interface between solid-state electrolyte and bulk Li is determined by the mechanically modified Butler–Volmer equation, which is the dominant principle for illustrating the relationship between overpotential and local current density.^[19,29,30] On the other hand, the mechanical failure of solid-state electrolyte is based on damage mechanics and fracture mechanics, involving stress, deformation, crack propagation in material.^[31,32]

First, Nernst–Planck equation was used to yield the flux of Li-ions for considering the electrodeposition of Li in the transient model:^[33–35]

$$N = -D\nabla c - q_{\text{Li}^+} u F c \nabla \eta_s \quad (1)$$

where N , D , c , u , and η_s are the transfer vector, the diffusion coefficient, the concentration of Li-ion in solid-state electrolyte, the ionic mobility, and the potential, respectively. q_{Li^+} is the charge of the Li-ion and F is the Faraday constant. The reaction for electrodeposition of Li can be described with the single-electron reduction of Li-ion:



The electrochemical kinetics of Equation 2 can be given with the modified Butler–Volmer equation to correlate the local current density with overpotential induced by stress:^[29,30]

$$i = i_0 \left[\exp\left(\frac{\alpha F}{RT} \Phi\right) - \exp\left(-\frac{\beta F}{RT} \Phi\right) \right] \quad (3)$$

where i_0 is the exchange current density, α and β are the anodic and cathodic transfer coefficients, respectively, and Φ is the overpotential and expressed as:^[36]

$$\Phi = \eta_s + \eta_m + \Delta\mu_{e^-} \quad (4)$$

Here η_s is the surface overpotential and η_m is the overpotential of mass-transfer. $\Delta\mu_{e^-}$ is the mechanical factor related to the electrochemical potential change induced by the local strain ($\Delta\mu_{e^-}$) and it is proposed according to the theory from Monroe and Newman as:^[29,30]

$$\Delta\mu_{e^-} = -\frac{1}{2} (\bar{V}_{Li} + t_- \bar{V}_{Li^+}) \times \{-2\gamma\kappa + n [\tau_d^{Li} - \tau_d^{LAGP}]\} + \frac{1}{2} (\bar{V}_{Li} - t_- \bar{V}_{Li^+}) (\Delta p_{Li} + \Delta p_{LAGP}) \quad (5)$$

where \bar{V}_i is related molar volume and γ is surface energy. κ is mean curvature, n is unite vector pointing from Li to bulk solid-state electrolyte, τ_d is the deformation stress while p is pressure.

Next, the fracture process of solid-state electrolyte induced by Li plating at interface is described by a damage model coupling cohesive zone model derived from the framework of fracture mechanics and continuum approach for crack propagation.^[19,31,32] The von Mises stress and equivalent strain are used as criterion for damage formation and crack propagation. Here, the stress (σ) and displacement of crack propagating (ℓ) can be expressed as:^[19,37]

$$\sigma = \sigma_0 \exp\left(-\frac{\sigma_0}{G} \ell\right) \quad (6)$$

where σ_0 is the initially uniaxial stress without displacement ($\ell = 0$) and G is fracture energy. Based on the damage model, the initial strain (ϵ_0) from the damage is defined as:

$$\epsilon_0 = \frac{\sigma_0}{E} \quad (7)$$

where E is Young's modulus of solid-state electrolyte. And the displacement of crack propagation is given as the product between strain change and the growth of damage in extending direction (h):

$$\ell = (\epsilon - \epsilon_0) h \quad (8)$$

Therefore, Equation 6 can be yielded as:

$$\sigma = \epsilon_0 E \exp\left(-\frac{\epsilon_0 E h}{G} (\epsilon - \epsilon_0)\right) \quad (9)$$

As seen in the Equation 9, the interfacial damage of the solid-state electrolytes caused by the crack propagation inside is associated with the development of Li filament in extending direction. Meanwhile, the growth of Li filament inside the solid-state electrolyte is also governed by the surrounding stress field which results in the shift of electrochemical potential. To sum up, the damage of solid-state electrolytes and the electrochemical deposition of Li inside defect or electrolyte are intimately coupled in this electro-chem-mechanical model.

3. Results and Discussion

The defects on solid-state electrolyte surface have been reported as round holes,^[24,38] pyramidal flaws,^[39,40] square pit,^[41,42] and irregular pores^[43,44] by using experimental methodologies. The geometries of those defects are strongly dependent on the size distribution of batch powder,^[45] sintering additive,^[38,39] and key parameters of sintering process, including sintering temperature,^[38,40,41] sintering time,^[40] applied pressure,^[24] sintering atmosphere,^[24] etc. Scanning electron microscope (SEM) is used to show the typical shapes of defects on solid-state electrolyte, as seen in Figure S1 (Supporting Information). In this work, the interfacial defects on the surface of solid-state electrolyte are built with typical geometries, including semi-sphere, semi-ellipsoid, pyramid and cube, to investigate the damage process of electrolyte induced by the continuous electrodeposition of Li in the defect after filling it (Table S1, Supporting Information). The distribution of von Mises stress shown in Figure 2a–d indicates that the profiles of the Li filaments deposited in defects witness the reinforced stress which is created by the compression in axial and circumferential. As shown in Figure S2 (Supporting Information), the stress field surrounding plated Li in the semi-spherical defect is relatively isotropic at the initial stage. As the Li filament's growing, the fluctuation of stress field gradually appears at the outside region of isotropic area, and it is more aggressive at the top of the semi-sphere (Figure 2a). Consequently, two separated secondary stress regions with butterfly-like shape are found outside the high-stress region. Furthermore, the local concentration of stress arises at the tip of defect with a sharp transmission into the bulk solid-state electrolytes, which contain defects with geometry of semi-ellipsoid, pyramid, and cube (Figure 2b,c). The concentration strength of stress is greater with semi-ellipsoidal defect than that with pyramidal defect with the same calculation time of 12s. As shown in Figure 2d and Figure S2m–p (Supporting Information), the concentrated stress field arises at two corners of cubic defect, showing a symmetric configuration at the initial calculating time. However, the differences of von Mises stress between two tips are triggered by dynamic meshing at the deformation boundary and thus the symmetry of the stress field is gradually fading. Both pyramidal and cubic defects have one or two tips and thus the angle of tip can be used to measure the sharpness of defects. Here, it is 90° for cubic defect, and 26.4° for pyramidal defect in Figure 2c,d. A region at position of $Y = 5 \mu\text{m}$ with width of $1 \mu\text{m}$ (marked in Figure 2a–d) is extracted for investigating the distribution of von Mises stress in the solid-state electrolyte near surface. The strength of the stress field in the side area increases with the sharp tip of interfacial defects, varying from semi-sphere to cube (Figure 2e). Moreover, the stress field in the middle area is much stronger with presence of cubic defect. For an overall evaluation of stress in solid-state electrolyte, the maximum of von Mises stress from semi-spherical defect is 24.1 MPa, which is the smallest among, while 147.1 MPa from semi-ellipsoidal defect, 61.2 MPa from pyramidal defect and 126.4 MPa from cubic defect are obtained. (Figure 2f). A precise statistic for the distribution of von Mises stress filed (Figure 2g) shows that the majority of stress is located at interval of low value. With the decreasing concentrated level associated with the lowering sharpness of defect tip (from cube to semi-sphere), the distribution of stress is

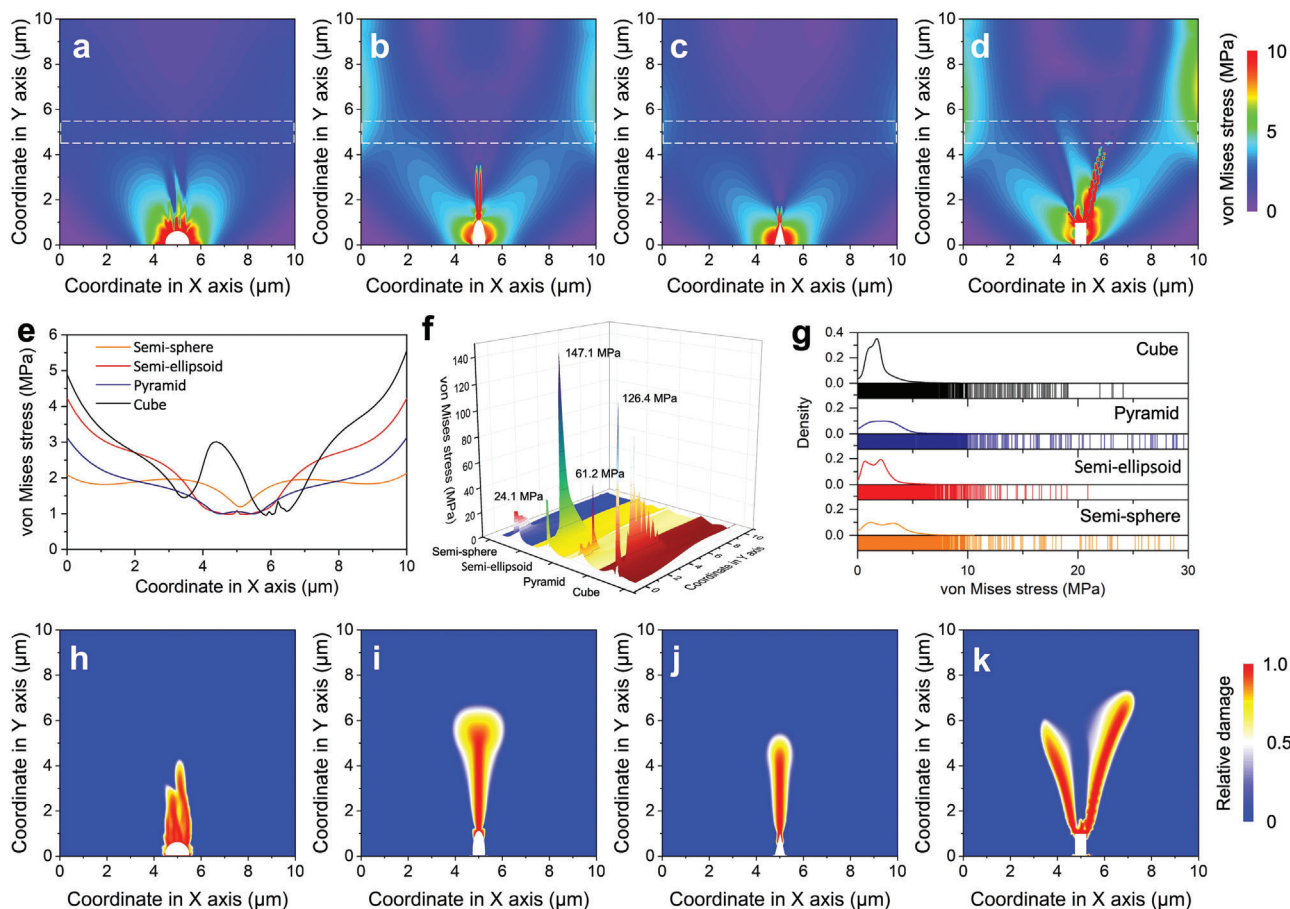


Figure 2. Distribution of stress and damage in solid-state electrolyte with interfacial defects of various geometries. Visualization of von Mises stress around Li filled defects with geometry of a) semi-sphere, b) semi-ellipsoid, c) pyramid, and d) cube. e) Distribution of von Mises stress along the middle region at position of $Y = 5 \mu\text{m}$ as marked by white dashed line in (a-d) and the width is $1 \mu\text{m}$. f) Contour map and g) numerical statistics of the stress field raised in solid-state electrolyte by continuous plating of Li in interfacial defects. Relative damage of solid-state electrolyte induced by the Li plating in the interfacial defects with geometries of h) semi-sphere, i) semi-ellipsoid, j) pyramid, and k) Cube. The calculation time for all figures is 12s.

gradually divided into two peaks or even flat plateau, demonstrating more even stress field inside the solid-state electrolyte.

As indicated in Equation 9, the accumulation of damage in solid-state electrolyte is resulted from the evolution of stress field during the Li plating in interfacial defects. The damaging regions of solid-state electrolyte formed with various defects are shown in Figure 2h–k. Three kinds of damaging regions are found, including flame-like shape from isotropic semi-spherical defect, rod shape from the semi-ellipsoidal and pyramidal defects, and splitting branch shape from the cubic defect. It is worth noticing that the configurations of these damage regions are initiated at very early stage of calculation and the propagation rate is strongly related to the geometry of defect on the surface of solid-state electrolyte (Figure S3, Supporting Information). The accumulation of relative damage will trigger formation of crack once it exceeds the tolerance of solid-state electrolyte. Therefore, the area of crack formation is totally buried in the damage regions and exhibits similar configuration with that for concentrated stress field (Figure S4, Supporting Information). Subsequently, the sum damage and corresponding sum crack were derived from the evolution within same calculation time of 12s, see Figure S5 (Supporting

Information). Greater damage caused by the development of Li filament in interfacial defects with geometries of semi-ellipsoid and cube as compared with that for semi-spherical and pyramidal defects. However, the crack generated from the semi-ellipsoidal defect is the greatest among others, following by the cubic, pyramidal, and semi-spherical defects. It suggests that the damage behavior of the solid-state electrolyte with interfacial defect is resulted from the stress field during the developing of Li filament in the defect region and both the damage propagation and crack formation are intimately associated with the geometry of defect.

A total failure of solid-state electrolyte in mechanics is found after various calculation time, as shown Figure S6 (Supporting Information). The failure time for disintegration of solid-state electrolyte with defect of semi-sphere, semi-ellipsoid, pyramid and cube is 37.6s, 13s, 25.8s, and 12.8s, respectively. At the convergence stage, the stress concentration region at the top of semi-spherical and pyramidal defects is much greater than that with semi-ellipsoidal and cubic defect (Figure S7, Supporting Information). Moreover, the region of the stress concentration started from the top of semi-spherical defect and transmit to form a twisted profile with enlarged area, which can be explained as the

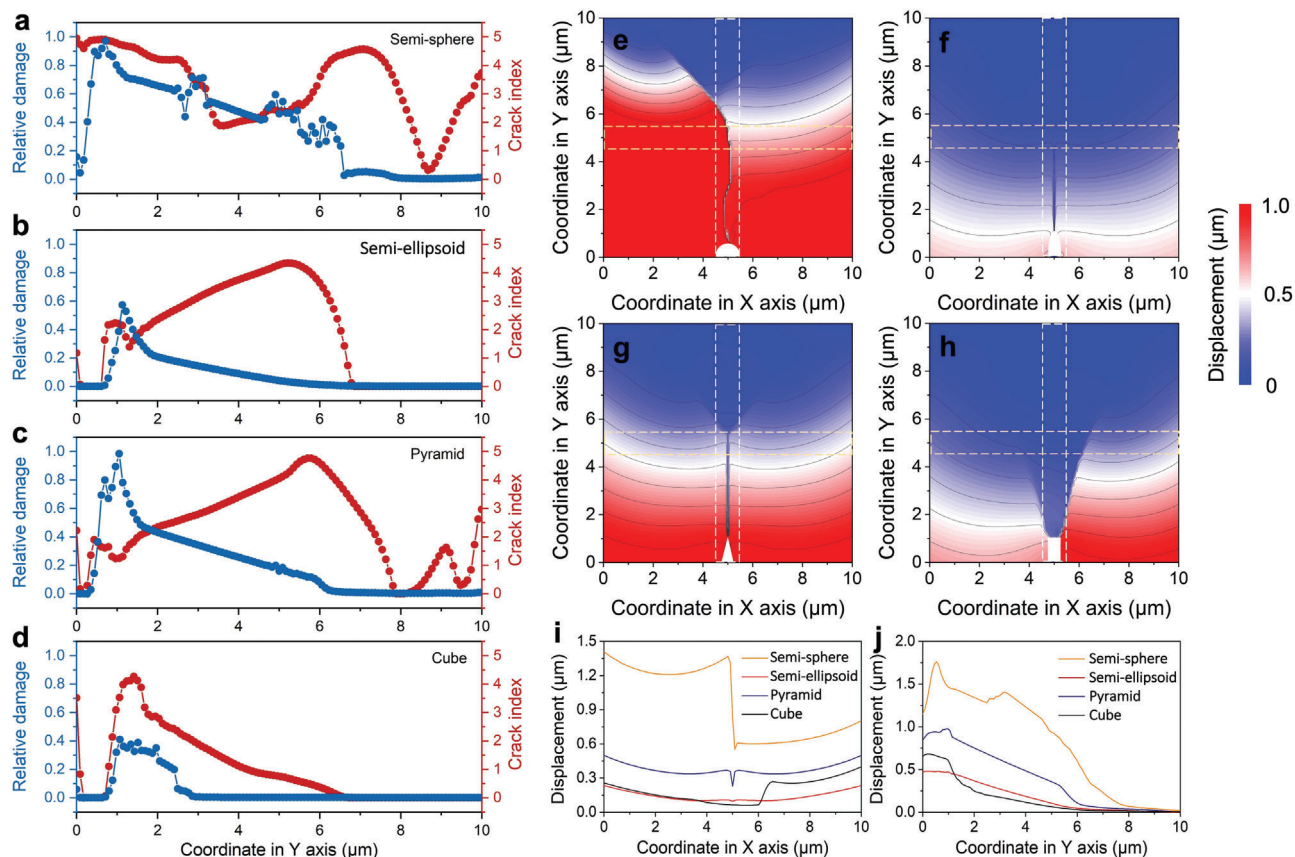


Figure 3. Mechanical failure of solid-state electrolyte with various defects under the continuous plating of Li at interface. Relative damage and corresponding crack along the middle region at position of $X = 5 \mu\text{m}$ with width of $1 \mu\text{m}$ in solid-state electrolyte which contains a) semi-spherical, b) semi-ellipsoidal, c) pyramidal, and d) cubic defect, respectively. Local displacement of solid-state electrolyte caused by Li plating in the interfacial defect with geometry of e) semi-sphere, f) semi-ellipsoid, g) pyramid, and h) cube. Distribution of displacement along i) the region at position of $Y = 5 \mu\text{m}$ and j) the region at position of $X = 5 \mu\text{m}$. These regions are marked by white dashed lines in (e–h) and the width is $1 \mu\text{m}$.

extension of local fluctuation from the stress field at the calculating time of 12s (Figure 2a). Therefore, enhanced damage region is obtained in the solid-state electrolyte with semi-spherical defect as the accumulation consequence of stress field, as seen in Figure S8 (Supporting Information). The damage region formed with pyramidal defect also shows extension to branch configuration at the convergence stage. By contrast, the final damage regions inside solid-state electrolyte with semi-ellipsoidal and cubic defects are similar with that at calculation time of 12 s. The propagation of crack in solid-state electrolyte with semi-spherical defect and pyramidal defect also is heavily accelerated during the calculation time after 12s (Figure S7, Supporting Information).

For a quantitative comparison of the damage and crack formed with various defects, a specific region at the position of $X = 5 \mu\text{m}$ with width of $1 \mu\text{m}$, which is vertical to the surface of Li anode, is extracted and plotted in Figure 3a–d. The high damage (>0.5) region formed with semi-spherical defect propagates to the middle of the solid-state electrolyte at the position of $Y = 5 \mu\text{m}$, and even extends to $Y = 6.5 \mu\text{m}$. The corresponding crack shows a relatively high value till $Y = 6.5 \mu\text{m}$ except a weakening region at position of $Y = 3.2$ to $5 \mu\text{m}$. Similarly, the damage regions formed with semi-ellipsoidal and pyramidal defects witness a peak at position of $Y = 1 \mu\text{m}$ and a slow declining till $Y = 6 \mu\text{m}$ (Figure 3b,c). The

corresponding cracks show a propagation with increasing value along with the direction away from tip of defects and a sudden decrease at position of $Y = 5 \mu\text{m}$, indicating decaying of propagation rate. However, the crack formed with pyramidal defect shows a longer propagation pathway on solid-state electrolyte and thus there is slight increase of crack at position of $Y = 9 \mu\text{m}$. Considering the failure time, the final failure of electrolyte caused by Li plating in semi-ellipsoidal defect is much faster than that for the pyramidal defect. Weak damage and small crack are obtained in the region on top of cubic defect, which can be explained with the mismatching between their propagating direction and orientation of extracted region (Figure 3d; Figure S8, Supporting Information).

Furthermore, the disintegration of solid-state electrolyte caused by the Li plating in interfacial defects can be illustrated by visualization of the local displacement inside electrolyte. As shown in Figure 3e, the most catastrophic displacement with asymmetric configuration shows inside the solid-state electrolyte with semi-spherical defect. In addition, symmetric distribution of displacements is observed in solid-state electrolyte with semi-ellipsoidal defect and pyramidal defect (Figure 3f,g) due to the similar distribution of stress and damage. The distribution of displacement turns to be asymmetric again on top of cubic

defect when stress and damage are split at the local region (Figure 3h). An overall compassion indicates that the displacement along with the damage orientation (*Y*-axis) in the solid-state electrolyte with semi-spherical defect is greater than that with other defects, which is intimately associated to the failure time. Moreover, the middle regions at the positions of $Y = 5 \mu\text{m}$ and $X = 5 \mu\text{m}$ were taken out to discuss the disintegration of the bulk of solid-state electrolyte due to the Li plating in interfacial defects. As shown in Figure 3i,j, the greatest displacement difference between two sides separated by the crack formed with semi-spherical defect is up to $1 \mu\text{m}$ and the majority of displacement occurs at the region near electrolyte surface.

The above results suggest that the bulk failure of solid-state electrolyte originated from the Li plating in interfacial defect is strongly dependent on the geometry of defect. Specifically, the electrodeposition of Li in the defect results in compression at the solid-state electrolyte/Li interface, triggering the transmission of stress from tip of defect to the bulk of electrolyte. Consequently, the accumulation of damage occurs under the local concentration of stress field and then the crack is forming once the damage exceeds the tolerance of solid-state electrolyte, which leads to the final disintegration or failure of electrolyte. Within the same failure time, the damage and associated crack of the solid-state electrolyte with semi-ellipsoidal defect and cubic defect are greater than that with the semi-spherical defect and pyramidal defect. The semi-spherical defect seems to leave the lightest influence on the failure of solid-state electrolytes as compared with the other interfacial defects. Indeed, the final failure of solid-state electrolyte with semi-spherical defect is deteriorated as severe asymmetric disintegration of the bulk electrolyte due to the longest failure time. Thus, we propose that semi-spherical defect delivers long-term impact on the failing process of solid-state electrolytes, including slow propagation rate for crack and final catastrophic disintegration.

To further evaluate the impact of geometric parameters of surface defects on the electro-chemo-mechanical failure of solid-state electrolyte, the aspect ratio of pyramidal defect is selected and varied in the model. This is because pyramid is a typical configuration for defects on the surface of ceramic solid-state electrolyte and its aspect ratio can be easily correlated to the roughness of surface.^[40,46,47] The variation of aspect ratio is divided into two groups. The first group is from 0.2 to 1.0 (vertex angle varying from 136.4° to 53.1°) with the constant height and varied width (Figure 4a,b; Figure S9a–i, Supporting Information) while the second group is from 1.5 to 5.0 (vertex angle varying from 36.9° to 11.4°) with the constant width and increasing height (Figure 4c,d; Figure S9j–q, Supporting Information). When the pyramidal defect has the lowest aspect ratio of 0.2, the distribution of von Mises stress inside the solid-state electrolyte caused by Li plating shows radicalized configuration outside the relatively flat profile of defect, illustrating the enlarged interface that encounters the compression from Li filament (Figure 4a). As the aspect ratio increasing from 0.2 to 1.0, two main region of high stress field are observed by the extension from two edges of defect (Figure 4b). Moreover, the stress also transmits from the tip of defect to the deep bulk of solid-state electrolyte, forming a *Y*-shape stress concentration region. Surprisingly, the high stress field originated from both edges and tip of pyramid shows a remarkable decaying when the aspect ratio increases to 2.0 (vertex

angle as 28.1° , Figure 4c). With more heightening of defect, the concentrated stress field from the edges is enhanced again and hotspots are found at the side of model (Figure 4d). It is worth noticing that the transmission of the stress concentration region from tip of defect shows an offset from the midline and it might be guided by the high stress region on the side.

Distribution of von Mises stress around pyramidal defects with various aspect ratios is further plotted in Figure 4e, showing the range of stress. A similar tendency for high stress field in visualization images is obtained and there is a steady increasing of von Mises stress when the aspect ratios is tuned from 0.25 to 1.0 (vertex angle varying from 126.9° to 53.1°). Importantly, the maximum stress witnesses a significant decrease as the aspect ratio rising to 2.0, and then the higher stress recovers with aspect ratio >2.5 (vertex angle as 22.6°). The frequency histograms (Figure 4f–h) present detailed features for the majority of von Mises stress in solid-state electrolyte with various defects. The majority of von Mises stress induced by Li plating in pyramidal defect with aspect ratio of 0.2 is <10 MPa and the frequency of the region between 5 and 10 MPa obviously rises as the aspect ratio increase from 0.25 to 1.0. However, the high frequency for this region almost vanishes when the aspect ratio is 2.0 and subsequently appears again as the following increase of aspect ratio.

The difference in distribution of von Mises stress in solid-state electrolyte will invariably lead to the variation of damage created. As seen in Figure 5a, branched region of damage with multiple propagating directions is obtained near the pyramidal defect with the aspect of 0.2, which may lead to the surface pulverization of solid-state electrolyte. A *Y*-shape region of damage with a main propagating direction is gradually emerging and dominates the distribution while the aspect ratio of defect varies from 0.2 to 1.0 (Figure 5b; Figure S10a–i, Supporting Information). Furthermore, when the pyramidal defect is elongated from the aspect ratio of 1.0 to 2.0 (vertex angle varying from 53.1° to 28.1°) with the constant width, the branched region of damage near the tip of defect is absent, and the rod shape region of damage shows up (Figure 5c; Figure S10j,k, Supporting Information). However, the end of damage region shows splitting configuration again when the aspect ratio is >2.5 (Figure 5d; Figure S10l–q, Supporting Information).

Furthermore, the values of relative damage along the propagating direction (*Y*-axis) are plotted as two groups mentioned above, see Figure 5e,f. Two regions with relative damage of 1, that is named as full damage, are observed at the position of $Y = 0–2 \mu\text{m}$ and $Y = 6–7.5 \mu\text{m}$ and they are bridged by the middle level damage region of 0.5. The full damage region near the tip of defect shows a shrinking shift to lower position when the aspect ratio increases from 0.2 to 1.0, which is consistent with the absence of branched regions in visualizing images. Importantly, the position of full damage region in the bulk of solid-state electrolyte shifts from $Y = 7.5 \mu\text{m}$ to $Y = 6 \mu\text{m}$, indicating the less propagating depth of damage in electrolyte with the increasing aspect ratio till 1.0. When the aspect ratio of pyramidal defect further rises from 1.5 to 5.0, one region of high damage and another one of full damage appear, as shown in Figure 5f. For the region near the tip of defect ($Y < 3 \mu\text{m}$), the damage is significantly reduced in the solid-state electrolyte with the aspect ratio of 2.0 for pyramid and then increases as the result of rising aspect ratio. Moreover, the region formed by propagation of damage into bulk of solid-state

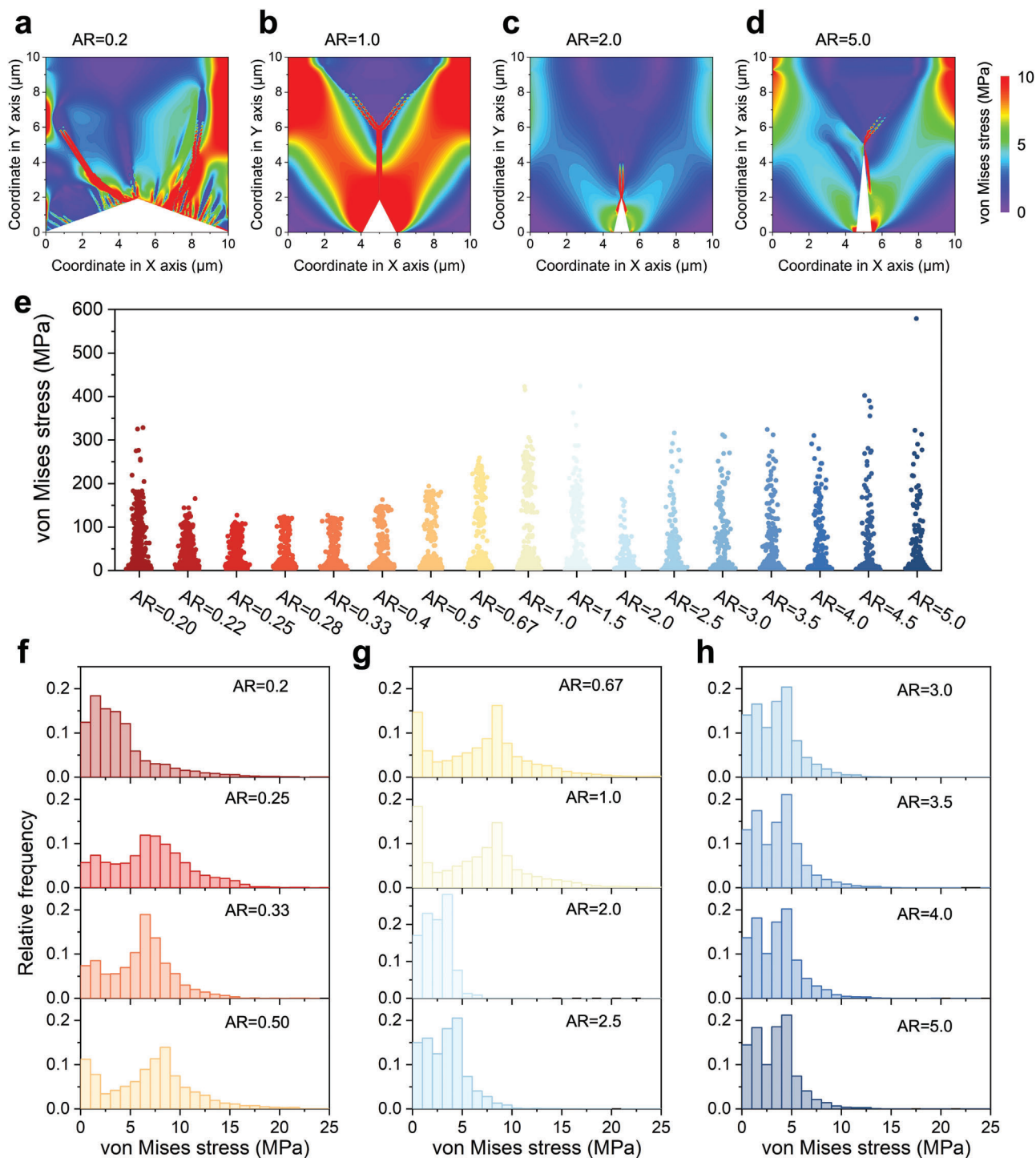


Figure 4. Distribution of von Mises stress around Li filled pyramidal defects with various aspect ratios. Visualization of von Mises stress inside solid-state electrolyte with pyramidal defects with the aspect ratio (AR) of a) 0.2, b) 1.0, c) 2.0, and d) 5.0 at convergence stage. e) Range of von Mises stress induced by Li plating in pyramidal defects with a series of aspect ratios. Frequency histograms for distribution of von Mises stress inside solid-state electrolyte containing interfacial defects with f) low, g) medium, and h) high aspect ratios.

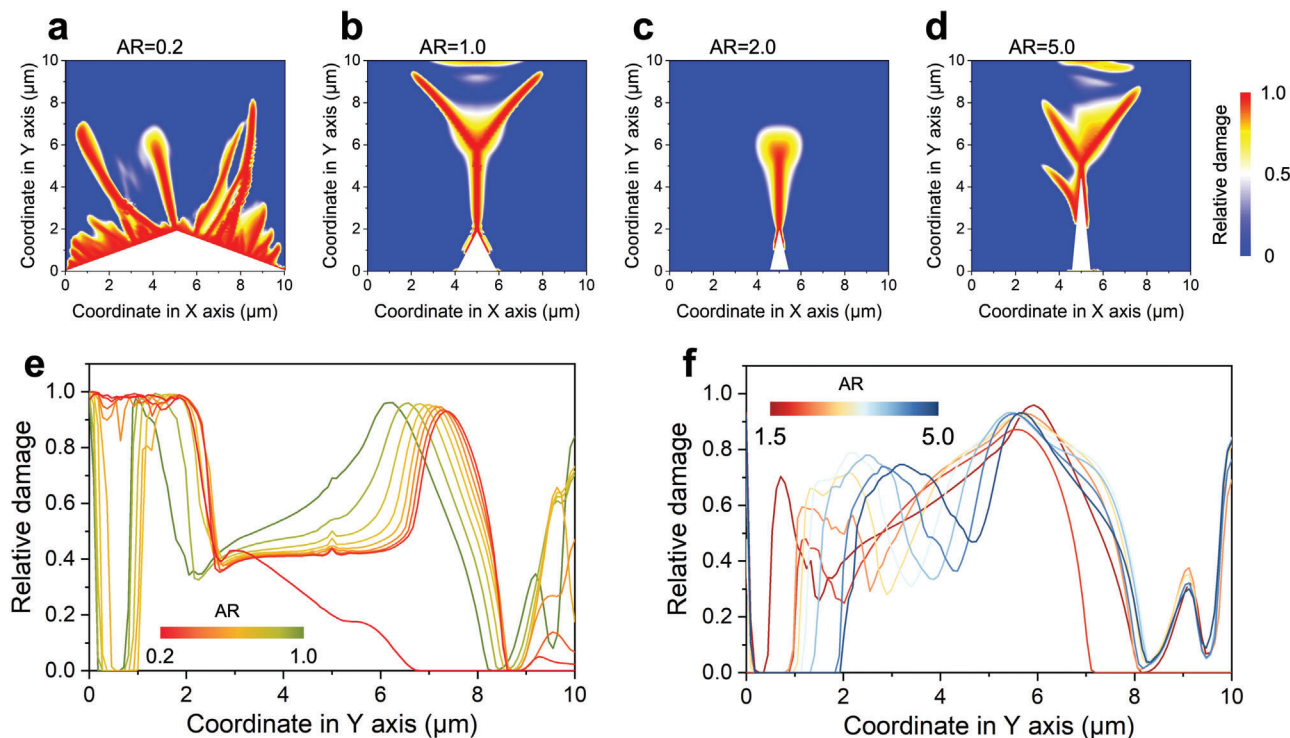


Figure 5. Role of defect aspect ratio on the damage of solid-state electrolyte induced by Li plating at interface. Visualization of damage derived from interface defects with aspect ratio of a) 0.2, b) 1.0, c) 2.0, and d) 5.0 at convergence stage. Distribution of relative damage along the line at the center of defects with aspect ratio ranging from e) 0.2 to 1.0 and f) 1.5 to 5.0.

electrolyte ($Y = 5\text{--}7\ \mu\text{m}$) shows a slight shift toward Li/solid-state electrolyte interface with aspect ratio of 2.0, suggesting less accumulation of damage. At the same time, no dramatic difference is present in this region for the pyramidal defects with other aspect ratios.

The disintegration of solid-state electrolytes caused by the accumulation of damage is revealed by the local displacement near the defect and in the bulk electrolyte. As shown in Figure 6a–d, two parts of the solid-state electrolyte are separated by the pyramidal defects and move oppositely under the continuous electrodeposition of Li in defect. Symmetric or quasi-symmetric distribution of the local displacement of solid-state electrolyte is obtained with the aspect ratio from 0.2 to 5.0. However, the region of high local displacement shows a tendency of shifting away from interface when the aspect ratio rises 0.2 to 1.0, whereas the high local displacement region shifts toward interface with aspect ratio of 2.0, indicating low displacement in the bulk of electrolyte (Figure 6e,f; Figure S11, Supporting Information). Next, the high local displacement is observed again in the region far from defect when the aspect ratio is >2.0 , see Figure 6f. The impact of aspect ratio on local displacement strongly agrees with the distribution of stress and damage. On the other hand, the accumulation of damage will also trigger the formation of cracks and their propagation in solid-state electrolyte, as seen in Figure S12 (Supporting Information). When the aspect ratio is <0.5 (vertex angle as 90°), multiple cracks form at the two edges of pyramid and propagate into the solid-state electrolyte. Meanwhile, the main crack generated near the tip of defects propagates along the midline of defect and secondary cracks form at end of main crack, showing

a deep propagation through the electrolyte (Figure 6g). It is worth noticing that the area of secondary cracks remarkably decreases following the aspect ratio from 1.0 to 2.0 (Figure 6h). Then, the secondary cracks are intimately regulated by the high stress region on the side of model. Therefore, both cracks formed near the edges of defect and secondary cracks formed in the depth of solid-state electrolyte are suppressed following the higher aspect ratio of pyramidal defect. This internal relationship could be useful for practical production of solid-state electrolytes.

To summarize the impact of defect aspect ratio on the mechanical failure of solid-state electrolyte, the sum damage and sum crack originated from various defects were calculated and plotted in Figure 6i. Two minima for both parameters are obtained when the aspect is 0.33 (vertex angle as 113.2°) in range of 0.2–1.0 and 2.0 in range of 1.5–5.0, whereas two maxima show up when aspect is 1.0 and 3.5. The tendency for sum damage and sum crack is significantly consistent with previous results for distribution of stress, damage, and displacement. The failure time and sum displacement in electrolyte (Figure 6j; Figure S13, Supporting Information) reveal that the solid-state electrolyte containing pyramidal defect with aspect ratio of 2.0 delivers longest failure time and lightest damage effect on the disintegration of electrolyte.

Our results reveal the role of interfacial defect on the mechanical failure of solid-state electrolyte which is induced by the electrochemical deposition of Li inside the defect. Both the geometry configuration and geometric parameter of the defect are critical to the concentration of von Mises stress, local displacement, and damage in the regions near the defect and inside bulk electrolyte as well. Previous X-ray computed tomography

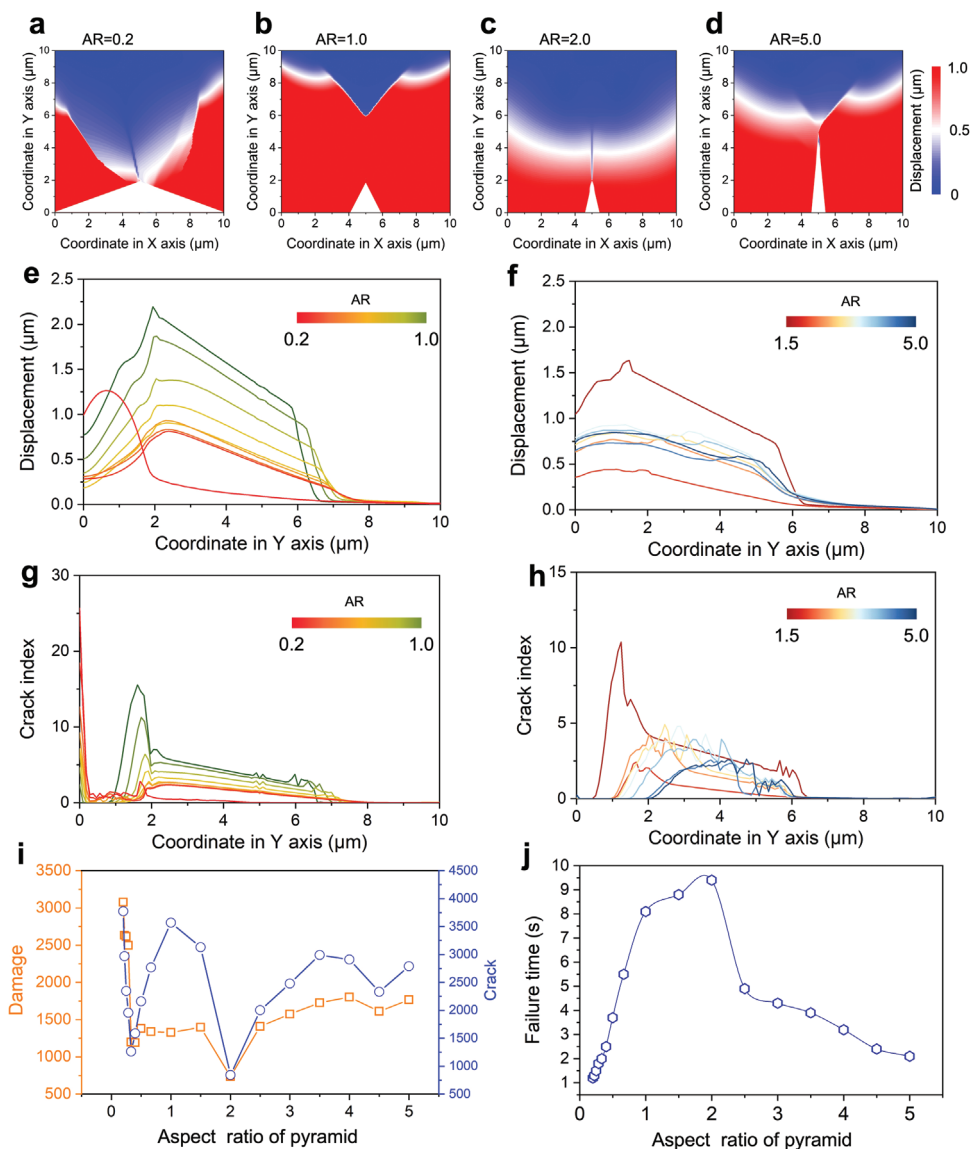


Figure 6. Role of defect aspect ratio on the mechanical failure of solid-state electrolyte. Visualization of displacement of solid-state electrolyte caused by Li plating in pyramidal defects with the aspect ratio of a) 0.2, b) 1.0, c) 2.0, and d) 5.0 at convergence stage. Distribution of displacement along the line at the center of defects with aspect ratio ranging from e) 0.2 to 1.0 and f) 1.0 to 5.0. Distribution of crack in solid-state electrolyte along the line at the center of defects with aspect ratio ranging from g) 0.2 to 1.0 and h) 1.0 to 5.0. i) Relative damage and the resulted crack inside solid-state electrolyte with various pyramidal defects on surface. j) Relationship between failure time of solid-state electrolyte and aspect ratio of interfacial defects.

results also suggest that the higher local current density, such as near solid-state electrolyte/Li interface edge, will induce high local stress and thus the cracks form as cone-shaped region to relieve stress.^[11,12,48] Moreover, the propagation of crack is found to be the extension of tip and continued deposition of Li further drives the propagation process.^[12,48] Therefore, the failure process of solid-state electrolyte captured by experimental methodologies are quite similar to that shown in this work. In situ electron microscopic methodologies and focused ion beam milling reveal that the 1D and 2D defects on solid-state electrolyte surface are potentially localized hot spots for Li deposition, promoting the penetration of Li filaments beneath these defects.^[24,27,49] This is consistent with the accumulation of damage and initia-

tion of crack inside defects on solid-state electrolyte, as shown in our results.

Therefore, a comprehensive comparison of results from our model with experimental data will show the correctness of the model, promising the application of the modeling results in practical design of interface for future solid-state batteries. Experimental data of X-ray computed tomogram of LAGP pellet during cycling in a Li/LAGP/Li cell,^[11] is used to build our model (Figure S14, Supporting Information), and then the calculation is carried out under the conditions applied in the experiment. The modeling results at the corresponding stages, regarding the capacity of deposited Li in the electrolyte pellet, are extracted and compared with the experimental results reported in this

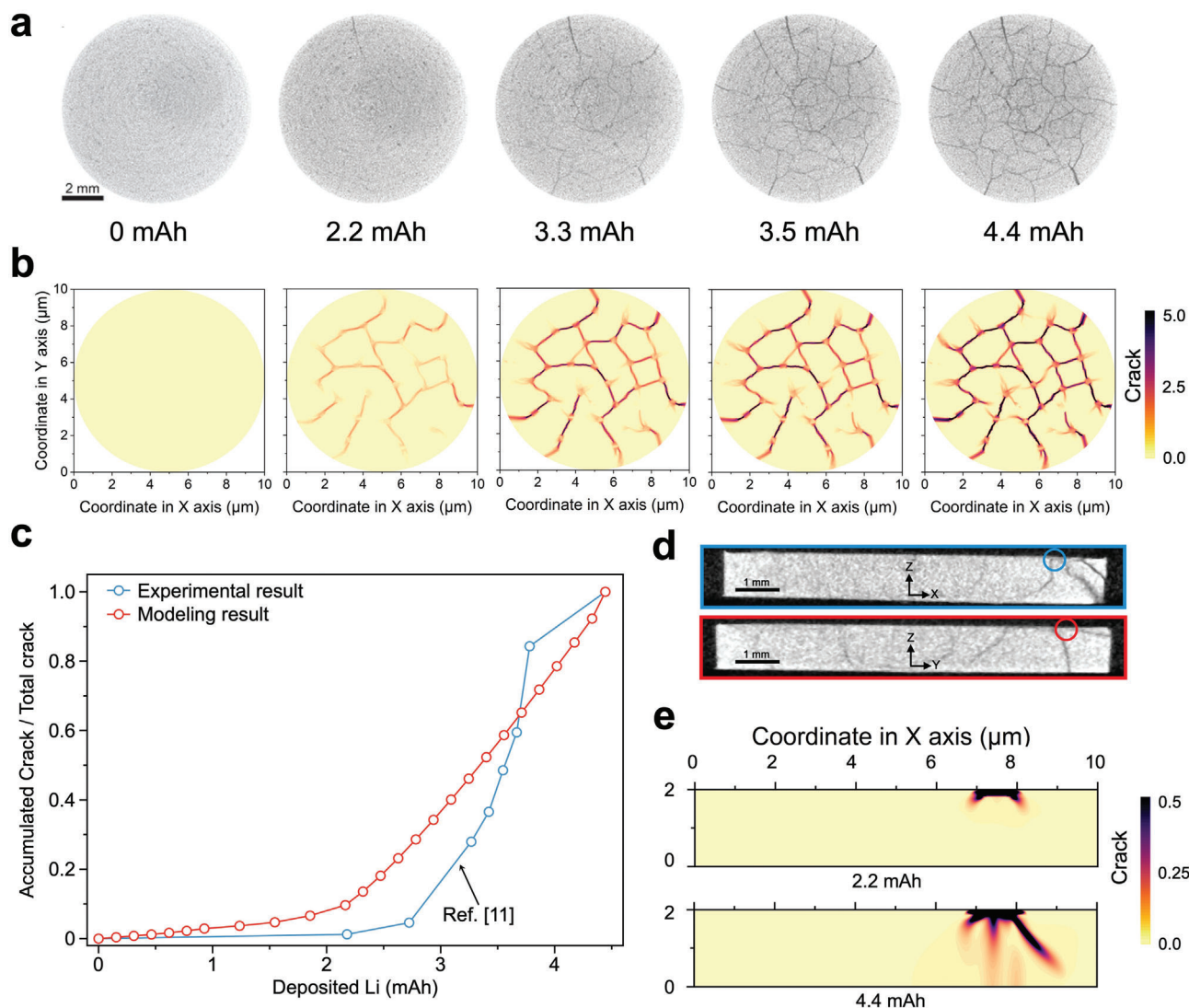


Figure 7. Comparison of modeling results with previous experimental data. a) Slices extracted from X-ray computed tomogram of LAGP pellet with increasing capacity of deposited Li. b) Modeling results for crack propagation inside solid-state electrolyte. c) Comparison of the accumulated cracks captured by in situ X-ray computed tomography and simulated by our model. d) Cross-sectional slices of LAGP pellet at a position with high local field. e) Modeling results for crack penetration through LAGP pellet during the deposition of Li in interfacial defect. a,d) Reproduced with permission.^[11] Copyright 2019, American Chemical Society.

publication,^[11] as shown in **Figure 7**. The crack formation has been successfully tracked by the X-ray computed tomogram of LAGP pellet with increasing capacity of deposited Li from 0 to 4.4 mAh (**Figure 7a**) until the thorough failure of electrolyte. The similar trend of crack formation in LAGP pellet is found in the modeling results at the same stages (**Figure 7b**; **Figure S15**, Supporting Information). Both experimental data and modeling results indicate that the massive formation of cracks occurs after a considerable amount of deposited Li, that is, half amount of total deposited Li. This suggests that the initial disposition of Li in solid-state electrolyte will not immediately induce severe degradation of electrolyte though the local stress and damage have been triggered inside, which are shown in the corresponding modeling results (**Figures S16 and S17**, Supporting Information). Following the increase of Li capacity, a remarkable rising for accu-

mulated cracks has been seen in experimental results (**Figure 7c**) while a sharp growth of cracks in modeling data also appears after the capacity of deposited Li > 2.0 mAh. To understand the impact of high local stress at LAGP/Li interface on the failure process of electrolyte, the experimental data showed cross-sectional slices, revealing the crack propagation through LAGP pellet (**Figure 7d**). A typical cubic defect in this work is created on the model to simulate the failure of solid-state electrolyte pellet caused by local high stress (**Figure S18**, Supporting Information). Transmission of concentrated stress and accumulation of damage from one side to another side are shown in the modeling results (**Figures S18 and S19**, Supporting Information). Moreover, the modeling results of crack propagation inside LAGP pellet (**Figure 7e**; **Figure S20**, Supporting Information) delivers similar pattern to that in experimental data.

Although our model shows a reasonable correctness when the results are compared with experimental data, the differences between them are also seen in Figure 7. For instance, more cracks are found in the calculated result with a capacity of 2.2 mAh and the curves for cracks accumulation are not closely overlapped. These differences are attributed to following reasons: i) In our model the solid-state electrolyte pellet is treated a continuum with isotropic properties and homogeneous distribution of material, whereas the real LAGP pellet has a random distribution of material and defects. ii) Experimental data of X-ray computed tomography is a 3D dataset and a certain slice may not be representative enough. iii) Partial parameters used in our model are from other literatures since they are missing in the work of X-ray computed tomography on LAGP pellet,^[11] potentially introducing deviation into the calculation process. iv) The interface conditions in real cell, including the high reactivity between LAGP and Li, varied properties of LAGP after lithiation,^[50,51] are more complicated and their impact on the electro–chemo–mechanical failure process of LAGP pellet is not negligible. Therefore, the correctness of model will be significantly improved if close coordination between modeling and experimental works is built in future.

Here, the mechanical behaviors of solid-state electrolyte during deposition of Li in interfacial defects, including stress concentration and transmission, damage accumulation and crack propagation, not only elucidate the evolution of electrolyte/Li interface, but also provide insightful perspectives for surface regulation of solid-state electrolyte in future SSLMBs. i) Avoid Li plating in interfacial defects. The results for mechanical failure of solid-state electrolyte demonstrate that the crack extension from defect to the bulk of brittle electrolyte is inevitable once the plating of Li in defect continues after filling it, regardless of geometry or parameter of defect. Therefore, the bottom-up approach to prevent this failure is separating the electrodeposition of Li away from the surface of solid-state electrolyte. One straightforward strategy is to fabricate an interlayer between solid-state electrolyte and Li anode, including metallic layer,^[52] zinc oxide layer,^[53] metal-organic frameworks-incorporated adhesive layer,^[42,54] ionic liquid paste layer,^[55] boron nitride layer,^[56] and polymer layer.^[57] However, designing an interlayer with sufficient ionic conductivity and good compatibility with both Li anode and solid-state electrolyte is still an as yet critical challenge. ii) Regulate surface pattern on solid-state electrolyte. Our results show that the interfacial defect with geometry of semi-sphere leads to less damage at the same calculation time, indicating high tolerance for the mechanical failure of solid-state electrolyte. This insight can be used as an inspiring reference for the strategies of surface regulation on solid-state electrolyte, such as 3D micropatterned surface on electrolyte.^[58] iii) Restrain presence of destructive defects. The surface defects on solid-state electrolyte can be well controlled or even totally removed by mechanical polishing^[7,23] or annealing for ceramic electrolytes.^[28] In this work, the results about impact of defect aspect ratio on the electro–chemo–mechanical failure of solid-state electrolyte reveal that the defect with low aspect ratio needs to be eliminated for suppressing the formation of cracks in solid-state electrolyte, which will potentially lead to a pulverization of electrolyte surface. Also, the defect with high aspect ratio (>3) may promote transmission of stress and propagation of cracks in the depth of solid-state electrolyte, bringing the risk

of Li filament penetration through the electrolyte, that is, internal short-circuit of cell.

4. Conclusion

In summary, we investigate the electro–chemo–mechanical failure of solid-state electrolyte induced by continuous electrodeposition of Li in interfacial defect by multiphysics simulation. The stress field generated by the compression from the growth of Li metal in the space of interfacial defect is concentrated at the structural fluctuation region, that is, the tip of the defect and then it transmits inward the solid-state electrolyte bulk to induce the accumulation of damage and local displacement in electrolyte. We show that the damage degree of solid-state electrolyte bulk is intimately associated with the geometry of interfacial defects and the defect of semi-sphere brings smallest damage in the same calculation time as compared with other geometries. Moreover, we studied the impact of geometric parameter of defect on the failure process of solid-state electrolyte and the aspect ratio of pyramidal defect is systemically examined for the distribution of von Mises stress, damage, and cracks. It is found that pyramidal defect with aspect ratio of 0.2–0.5 (vertex angle varying from 136.4° to 90°) leads to a radicalized configuration of stress field and thus creates branched region of damage, as well as crack near the interface. When the aspect ratio of defect rises from 1.0 to 2.0 (vertex angle varying from 53.1° to 28.1°), the propagation of damage and crack in solid-state electrolyte is remarkably suppressed due to the vanishing of high stress region that starts at the edge of pyramid. However, the high stress region far from interface can be triggered when the aspect ratio increases up to 3.0 (vertex angle as 18.9°) or even higher. Our results provide valuable standpoints for interlayer design and surface regulation to prevent the mechanical degradation of solid-state electrolyte induced by Li plating in interfacial defect, paving the way to achieve higher critical current density for SSLMBs under realistic conditions. Last but not the least, the understanding of metal filaments in defects of brittle solid materials are also of high importance for other research about solid state ionics, promising an interdisciplinary contribution.

5. Simulation Section

The construction of electro–chemo–mechanical model and the solution process were carried out by combination of electrochemical module and solid mechanics module in COMSOL Multiphysics software. The key parameters for the model building are listed in **Table 1** and the related theory has been described in previous section. Both MATLAB and Python were used for data analysis and visualization.

The structures of model are segmented by using an ultra-fine mesh with a maximum mesh size of 0.02 μm in an attempt to obtain a high accuracy solution. The key boundary conditions are set as follows: i) Both solid-state electrolyte and Li metal anode are set as isotropic solid material with stable mechanical and electrical properties. ii) The efficiency for electrodeposition of Li in interfacial defects is 100%, regardless of the occurrence of any side reaction. iii) 80% of the damage level is determined as the criterion for complete failure of solid-state electrolyte and the calculation

Table 1. Parameters used in the electro–chemo–mechanical model.

Parameters	Value
Anodic charge transfer coefficient	0.5
Cathodic charge transfer coefficient	0.5
Electronic conductivity of Li	11 000 000 S m ⁻¹
Density of Li metal	0.534 g cm ⁻³
Young's modulus of Li metal	4.9 GPa
Poisson's ratio of Li metal	0.36
Yield stress of Li metal	0.4 MPa
Ionic conductivity of LAGP	0.01 S m ⁻¹
Density of LAGP	3.52 g cm ⁻³
Young's modulus of LAGP	120 GPa
Poisson's ratio of LAGP	0.25
Faraday's constant	96485 C mol ⁻¹
Gas constant	8.314 J (mol K) ⁻¹
Temperature	300 K
Equilibrium potential	0.135 V
Exchange current density	0.01 mA cm ⁻²

time for the complete failure is defined as the failure time for disintegration of solid-state electrolyte. The ionic conductivity of solid-state electrolyte unit is set as 0 if the damage degree exceeds 80%, which is defined as the tolerance of solid-state electrolyte. Meanwhile the ionic conductivity of electrolyte unit is as a linear function of damage when the damage is <80%. iv) For solving the model with square configuration, the top side and bottom side of square are set as fixed boundaries and thus the deformation and displacement of solid material can only expand along the left or right directions, which is consistent with the realistic testing of solid-state electrolyte in a steel mold.

An idea interface is assumed here and the chemical reactions between solid-state electrolyte and Li^[39,59] is not considered in the model. The cathode is not considered here either. The initial state of electrochemical deposition of Li in this model is set as the filling of interfacial defect by Li filaments and the stress at the interface between Li and solid-state electrolyte is 0. The properties of solid-state electrolyte and Li anode are shown in Table 1. As the electrodeposition process of Li continues, the growth of Li filaments leads to the transmission of stress toward the solid-state electrolyte bulk, causing accumulation of damage in brittle electrolyte and generation of cracks, as well as displacement. The relative tolerance of the solution process was set as 0.0001, and the limit time for solving model was 50 units of calculation time.

Supporting Information

Supporting Information is available from the Wiley Online Library or from the author.

Acknowledgements

Y.L. and X.X. contributed equally to this work. This work was supported by the National Natural Science Foundation of China (no. 51802256) and the China Scholarship Council (no. 201908090043). The authors thank for the support from Chalmers Areas of Advance Materials Science and Energy and Batteries Sweden (BASE).

Conflict of Interest

The authors declare no conflict of interest.

Data Availability Statement

The data that support the findings of this study are available from the corresponding author upon reasonable request.

Keywords

electro–chemo–mechanics, interfacial defects, mechanical failure, solid-state batteries, solid-state electrolyte

Received: February 6, 2023

Revised: April 11, 2023

Published online:

- [1] Y. Zhu, J. C. Gonzalez-Rosillo, M. Balaish, Z. D. Hood, K. J. Kim, J. L. M. Rupp, *Nat. Rev. Mater.* **2021**, 6, 313.
- [2] M. Balaish, J. C. Gonzalez-Rosillo, K. J. Kim, Y. Zhu, Z. D. Hood, J. L. M. Rupp, *Nat. Energy* **2021**, 6, 227.
- [3] D. H. S. Tan, Y.-T. Chen, H. Yang, W. Bao, B. Sreenarayanan, J.-M. Doux, W. Li, B. Lu, S.-Y. Ham, B. Sayahpour, J. Scharf, E. A. Wu, G. Deysher, H. E. Han, H. J. Hah, H. Jeong, J. B. Lee, Z. Chen, Y. S. Meng, *Science* **2021**, 373, 1494.
- [4] R. J. Y. Park, C. M. Eschler, C. D. Fincher, A. F. Badel, P. Guan, M. Pharr, B. W. Sheldon, W. C. Carter, V. Viswanathan, Y.-M. Chiang, *Nat. Energy* **2021**, 6, 314.
- [5] Y. Lu, C.-Z. Zhao, H. Yuan, X.-B. Cheng, J.-Q. Huang, Q. Zhang, *Adv. Funct. Mater.* **2021**, 31, 2009925.
- [6] T. Dussart, N. Rividi, M. Fialin, G. Toussaint, P. Stevens, C. Laberty-Robert, *J. Electrochem. Soc.* **2021**, 168, 120550.
- [7] F. Flatscher, M. Philipp, S. Ganschow, H. M. R. Wilkening, D. Rettenwander, *J. Mater. Chem. A* **2020**, 8, 15782.
- [8] S. Sarkar, V. Thangadurai, *ACS Energy Lett.* **2022**, 7, 1492.
- [9] L. Porz, T. Swamy, B. W. Sheldon, D. Rettenwander, T. Frömling, H. L. Thaman, S. Berendts, R. Uecker, W. C. Carter, Y.-M. Chiang, *Adv. Energy Mater.* **2017**, 7, 1701003.
- [10] J. A. Lewis, F. J. Q. Cortes, Y. Liu, J. C. Miers, A. Verma, B. S. Vishnugopi, J. Tippens, D. Prakash, T. S. Marchese, S. Y. Han, C. Lee, P. P. Shetty, H. W. Lee, P. Shevchenko, F. De Carlo, C. Saldana, P. P. Mukherjee, M. T. McDowell, *Nat. Mater.* **2021**, 20, 503.
- [11] J. Tippens, J. C. Miers, A. Afshar, J. A. Lewis, F. J. Q. Cortes, H. Qiao, T. S. Marchese, C. V. Di Leo, C. Saldana, M. T. McDowell, *ACS Energy Lett.* **2019**, 4, 1475.
- [12] Z. Ning, D. S. Jolly, G. Li, R. De Meyere, S. D. Pu, Y. Chen, J. Kasemchainan, J. Ihli, C. Gong, B. Liu, D. L. R. Melvin, A. Bonnini, O. Magdysyuk, P. Adamson, G. O. Hartley, C. W. Monroe, T. J. Marrow, P. G. Bruce, *Nat. Mater.* **2021**, 20, 1121.
- [13] C. Sun, J. Liu, Y. Gong, D. P. Wilkinson, J. Zhang, *Nano Energy* **2017**, 33, 363.
- [14] G. Qiu, L. Lu, Y. Lu, C. Sun, *ACS Appl. Mater. Interfaces* **2020**, 12, 28345.
- [15] E. Kazyak, R. Garcia-Mendez, W. S. LePage, A. Sharafi, A. L. Davis, A. J. Sanchez, K.-H. Chen, C. Haslam, J. Sakamoto, N. P. Dasgupta, *Matter* **2020**, 2, 1025.
- [16] F. Han, A. S. Westover, J. Yue, X. Fan, F. Wang, M. Chi, D. N. Leonard, N. J. Dudney, H. Wang, C. Wang, *Nat. Energy* **2019**, 4, 187.
- [17] X. Zhang, C. Sun, *Phys. Chem. Chem. Phys.* **2022**, 24, 19996.

- [18] X. Liu, R. Garcia-Mendez, A. R. Lupini, Y. Cheng, Z. D. Hood, F. Han, A. Sharafi, J. C. Idrobo, N. J. Dudney, C. Wang, C. Ma, J. Sakamoto, M. Chi, *Nat. Mater.* **2021**, *20*, 1485.
- [19] X. Xu, Y. Liu, O. O. Kapitanova, Z. Song, J. Sun, S. Xiong, *Adv. Mater.* **2022**, *34*, 2207232.
- [20] A. Masias, N. Felten, R. Garcia-Mendez, J. Wolfenstine, J. Sakamoto, *J. Mater. Sci.* **2019**, *54*, 2585.
- [21] H.-K. Tian, Z. Liu, Y. Ji, L.-Q. Chen, Y. Qi, *Chem. Mater.* **2019**, *31*, 7351.
- [22] M. Yang, Y. Liu, A. M. Nolan, Y. Mo, *Adv. Mater.* **2021**, *33*, 2008081.
- [23] Q. Tu, L. Barroso-Luque, T. Shi, G. Ceder, *Cell Rep. Phys. Sci.* **2020**, *1*, 100106.
- [24] H. Wang, H. Gao, X. Chen, J. Zhu, W. Li, Z. Gong, Y. Li, M.-S. Wang, Y. Yang, *Adv. Energy Mater.* **2021**, *11*, 2102148.
- [25] Q. Tu, T. Shi, S. Chakravarthy, G. Ceder, *Matter* **2021**, *4*, 3248.
- [26] F. Sun, C. Wang, M. Osenberg, K. Dong, S. Zhang, C. Yang, Y. Wang, A. Hilger, J. Zhang, S. Dong, H. Markötter, I. Manke, G. Cui, *Adv. Energy Mater.* **2022**, *12*, 2103714.
- [27] J. H. Cho, K. Kim, S. Chakravarthy, X. Xiao, J. L. M. Rupp, B. W. Sheldon, *Adv. Energy Mater.* **2022**, *12*, 2200369.
- [28] R. DeWees, H. Wang, *ChemSusChem* **2019**, *12*, 3713.
- [29] C. Monroe, J. Newman, *J. Electrochem. Soc.* **2005**, *152*, A396.
- [30] C. Monroe, J. Newman, *J. Electrochem. Soc.* **2004**, *151*, A880.
- [31] M. Kurumatani, Y. Soma, K. Terada, *Eng. Fract. Mech.* **2019**, *206*, 392.
- [32] M. Kurumatani, K. Terada, J. Kato, T. Kyoya, K. Kashiyama, *Eng. Fract. Mech.* **2016**, *155*, 49.
- [33] Y. Liu, X. Xu, O. O. Kapitanova, P. V. Evdokimov, Z. Song, A. Matic, S. Xiong, *Adv. Energy Mater.* **2022**, *12*, 2103589.
- [34] C. Brissot, M. Rosso, J.-N. Chazalviel, P. Baudry, S. Lascaud, *Electrochim. Acta* **1998**, *43*, 1569.
- [35] J.-N. Chazalviel, *Phys. Rev. A* **1990**, *42*, 7355.
- [36] S.-L. Wu, A. E. Javier, D. Devaux, N. P. Balsara, V. Srinivasan, *J. Electrochem. Soc.* **2014**, *161*, A1836.
- [37] G. N. Wells, L. J. Sluys, *Eng. Fract. Mech.* **2000**, *65*, 263.
- [38] T. Hupfer, E. C. Bucharsky, K. G. Schell, M. J. Hoffmann, *Solid State Ionics* **2017**, *302*, 49.
- [39] A. Paoletta, W. Zhu, G.-L. Xu, A. La Monaca, S. Savoie, G. Girard, A. Vijn, H. Demers, A. Perea, N. Delaporte, A. Guerfi, X. Liu, Y. Ren, C.-J. Sun, J. Lu, K. Amine, K. Zaghib, *Adv. Energy Mater.* **2020**, *10*, 2001497.
- [40] E.-J. Yi, K.-Y. Yoon, H.-A. Jung, T. Nakayama, M.-J. Ji, H. Hwang, *Appl. Surf. Sci.* **2019**, *473*, 622.
- [41] K. Waetzig, A. Rost, U. Langklotz, B. Matthey, J. Schilm, *J. Eur. Ceram. Soc.* **2016**, *36*, 1995.
- [42] R. Zhao, L. Gao, M. Song, Y. Ye, Z. Liang, J. Bian, J. Zhu, S. Li, R. Zou, Y. Zhao, *ACS Energy Lett.* **2021**, *6*, 3141.
- [43] J. A. Lewis, F. J. Q. Cortes, M. G. Boebinger, J. Tippens, T. S. Marchese, N. Kondekar, X. Liu, M. Chi, M. T. McDowell, *ACS Energy Lett.* **2019**, *4*, 591.
- [44] K. Arbi, W. Bucheli, R. Jiménez, J. Sanz, *J. Eur. Ceram. Soc.* **2015**, *35*, 1477.
- [45] S.-H. Leigh, C. C. Berndt, *J. Am. Ceram. Soc.* **1999**, *82*, 17.
- [46] H. Wehbe, L. O. Schmidt, M. W. Kandula, K. Dilger, *Appl. Phys. A* **2022**, *128*, 889.
- [47] S. Duluard, A. Paillassa, L. Puech, P. Vinatier, V. Turq, P. Rozier, P. Lenormand, P.-L. Taberna, P. Simon, F. Ansart, *J. Eur. Ceram. Soc.* **2013**, *33*, 1145.
- [48] S. Hao, S. R. Daemi, T. M. M. Heenan, W. Du, C. Tan, M. Storm, C. Rau, D. J. L. Brett, P. R. Shearing, *Nano Energy* **2021**, *82*, 105744.
- [49] T. Krauskopf, R. Dippel, H. Hartmann, K. Peppler, B. Mogwitz, F. H. Richter, W. G. Zeier, J. Janek, *Joule* **2019**, *3*, 2030.
- [50] J. Yan, D. Zhu, H. Ye, H. Sun, X. Zhang, J. Yao, J. Chen, L. Geng, Y. Su, P. Zhang, Q. Dai, Z. Wang, J. Wang, J. Zhao, Z. Rong, H. Li, B. Guo, S. Ichikawa, D. Gao, L. Zhang, J. Huang, Y. Tang, *ACS Energy Lett.* **2022**, *7*, 3855.
- [51] J. Zhu, J. Zhao, Y. Xiang, M. Lin, H. Wang, B. Zheng, H. He, Q. Wu, J. Y. Huang, Y. Yang, *Chem. Mater.* **2020**, *32*, 4998.
- [52] V. Raj, V. Venturi, V. R. Kankanallu, B. Kuiru, V. Viswanathan, N. P. B. Aetukuri, *Nat. Mater.* **2022**, *21*, 1050.
- [53] X. Hao, Q. Zhao, S. Su, S. Zhang, J. Ma, L. Shen, Q. Yu, L. Zhao, Y. Liu, F. Kang, Y. B. He, *Adv. Energy Mater.* **2019**, *9*, 1901604.
- [54] T. Wang, X. Zhang, N. Yuan, C. Sun, *Chem. Eng. J.* **2023**, *451*, 138819.
- [55] S. Xiong, Y. Liu, P. Jankowski, Q. Liu, F. Nitze, K. Xie, J. Song, A. Matic, *Adv. Funct. Mater.* **2020**, *30*, 2001444.
- [56] Q. Cheng, A. Li, N. Li, S. Li, A. Zangiabadi, T.-D. Li, W. Huang, A. C. Li, T. Jin, Q. Song, W. Xu, N. Ni, H. Zhai, M. Dontigny, K. Zaghib, X. Chuan, D. Su, K. Yan, Y. Yang, *Joule* **2019**, *3*, 1510.
- [57] Z. Chen, G.-T. Kim, J.-K. Kim, M. Zarrabeitia, M. Kuenzel, H.-P. Liang, D. Geiger, U. Kaiser, S. Passerini, *Adv. Energy Mater.* **2021**, *11*, 2101339.
- [58] R. Xu, F. Liu, Y. Ye, H. Chen, R. R. Yang, Y. Ma, W. Huang, J. Wan, Y. Cui, *Adv. Mater.* **2021**, *33*, 2104009.
- [59] H. Chung, B. Kang, *Chem. Mater.* **2017**, *29*, 8611.